NeuroImage **17,** 1131–1143 (2002)
doi:10.1006/nimg.2002.1285

A Framework for Callosal Fiber Distribution Analysis

Dongrong Xu,*,† Susumu Mori,†,‡ Meiyappan Solaiyappan,† Peter C. M. van Zijl,†,‡ and Christos Davatzikos*,†

**Center for Biomedical Image Computing, †Department of Radiology and Radiological Science, and ‡F. M. Kirby Research Center for Functional Brain Imaging, Johns Hopkins University School of Medicine, Baltimore, Maryland 21287*

Received October 9, 2001

This paper presents a framework for analyzing the spatial distribution of neural fibers in the brain, with emphasis on interhemispheric fiber bundles crossing through the corpus callosum. The proposed approach combines methodologies for fiber tracking and spatial normalization and is applied on diffusion tensor images and standard magnetic resonance images.

Key Words: **corpus callosum; fiber tracking; probabilistic map; diffusion tensor imaging; interhemispheric connectivity.**

INTRODUCTION

To study development trends or changes in brain structure due to certain diseases, one usually needs to spatially normalize the subjects and create probabilistic maps, along a time axis, of this particular group of subjects for comparison. The probabilistic maps are statistics that reflect the probability of finding a particular structure at a given location, within a group of individuals. This procedure is widely used by the neuroimaging community as a means of characterizing abnormal pathological neuroanatomy of populations, because statistics over a group of individuals helps overcome two limitations of single-individual images. First, they represent the characteristics of an entire population, rather than of an individual, and therefore they can be used as normative data. Second, by averaging across individuals they tend to reduce noise or artifacts that are caused by the specimen preparation or imaging procedures. However, such probabilistic maps may represent only population trends and not individual deviations from these trends. The work of this paper presents a framework for elastic registration of a group of subjects to help study fiber distribution in white matter with emphasis on callosal fibers, by combining diffusion tensor image (DTI)-based fiber tractography and deformable registration methods. This framework is ready for construction of probabilistic maps in regions of interest (ROIs) and thus forms the basis for further analysis, by using any available tools such as SPM.

The corpus callosum was selected among other fiber bundles for three reasons. First, the projections of callosal fibers to the cortex have been studied extensively in the neuroanatomical literature (Thompson *et al.*, 1999; Bates and Elman, 1993). Second, DTI has been shown by several investigators to yield highly reproducible reconstructions of callosal fibers that are consistent with neuroanatomical knowledge (Mori *et al.*, 2000, 2001; Basser *et al.*, 2000; Poupon *et al.*, 2000). Finally, changes in regional callosal structure have been reported in a lot of diseases and disorders, such as Alzheimer's disease (Vermersch *et al.*, 1996; Janowsky *et al.*, 1996), attention deficit hyperactivity disorder (Giedd *et al.*, 1994; Baumgardner *et al.*, 1996), and schizophrenia (Woodruff *et al.*, 1993; Bookstein, 1996). Several studies have also investigated regional sex differences in the corpus callosum (Beaton, 1997; Bishop and Wahsten, 1997; Clarke *et al.*, 1989; Davatzikos *et al.*, 1996; Delacoste-Utamsing and Holloway, 1982), which presumably reflect underlying differences in interhemispheric connectivity.

In order to be able to interpret the functional implications of differences or changes in the callosal structure, and to better understand interhemispheric connectivity, we need certain practically computable frameworks for generating statistical maps of spatial distribution of fibers that cross through the corpus callosum. Such probabilistic maps can also be used to study how brain connectivity is affected by disease. Although many histopathological investigations have elucidated the structure of white matter projections from the corpus callosum to various cortical areas, DTI in conjunction with image analysis methods for tracking and spatial normalization of white matter fibers is very promising, primarily for two reasons. First, brain pathology as well as neural development and aging can be examined *in vivo* (Mori *et al.*, 2001, 2002; Stieltjes *et al.*, 2001). Second, large populations can be examined instead of small isolated cases. DTI was recently shown to elucidate changes in brain connectivity in studies of

1053-8119/02 $35.00

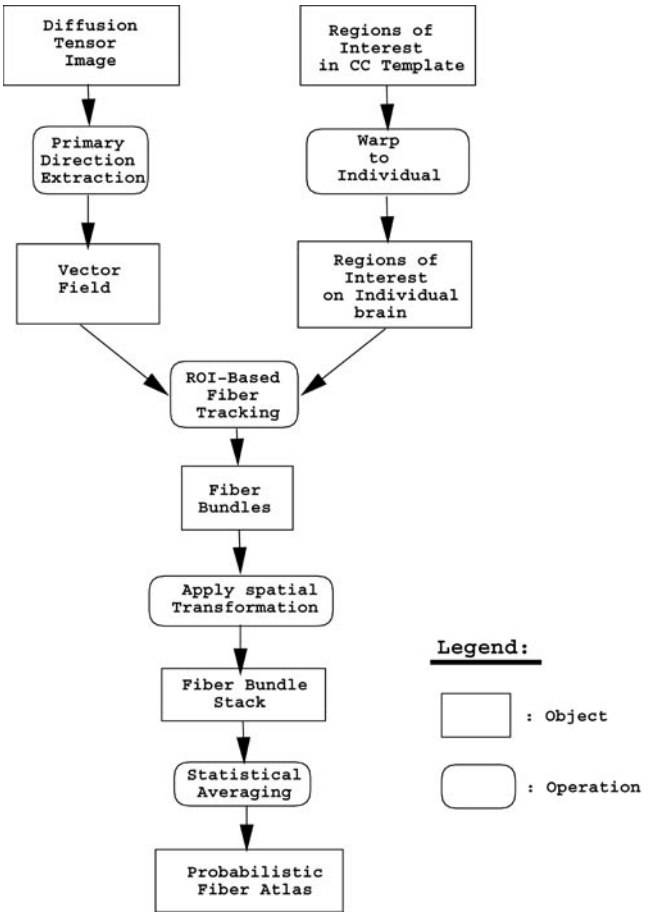

FIG. 1. Data flow of constructing a probabilistic map of callosal fibers using diffusion tensor imaging.

aging and development (O'Sullivan *et al.*, 2001; Mori *et al.*, 2001; Huppi, 2001; Neil *et al.*, 1998; Pfefferbaum *et al.*, 2000).

Traditional magnetic resonance images provide good contrast between gray matter, white matter, and cerebrospinal fluid (CSF). However, they provide no information about brain connectivity. Hence, they can be of little help in explaining how specific neural pathways can be affected by disease. Although modern image analysis techniques attempt to obtain regional volumetric measurements of white matter, they are inherently limited by the lack of structural detail within the white matter. In particular, regional changes in fiber bundles can be observed only indirectly, via changes of nearby structures that have sufficient contrast in MRI. In contrast, diffusion tensor images record microscopic water diffusion within neural fibers, averaged over voxel-sized regions. Since water molecules are restricted by the fiber walls, they diffuse preferentially along the fiber direction. Therefore, DTI provides adequate contrast for differentiation of several major fiber bundles, and it is bound to play an important role in elucidating brain connectivity from *in vivo* data.

A great deal of work has been done during the past several years on fiber tracking methods from DT images (Mori *et al.*, 1999, 2000, 2001; Conturo *et al.*, 1999; Stielties *et al.*, 2001; Poupon, *et al.*, 1998, 2000). Despite these efforts, several main challenges still remain, including complications at fiber intersections, noise that can cause early termination or deviation of tracking, and inadequate resolution of thinner cortical fibers. Unavoidably, errors in fiber reconstruction from DTI are to be expected. Our premise is that such errors can be greatly reduced by statistical averaging across subjects of the DTI data as well as the fibers reconstructed from them. Accordingly, only robust and consistent trends across individuals are retained in a probabilistic map.

An important aspect of setting up such a framework for generating probabilistic maps is spatial normalization, i.e., the procedure used to remove gross interindividual anatomical variability, thus allowing the investigation of variability in brain connectivity and in particular in fiber pathways. A large body of literature exists on developing probabilistic atlases of brain structure (Greitz *et al.*, 1991; Miller *et al.*, 1993; Evans *et al.*, 1993; Gee *et al.*, 1993; Roland *et al.*, 1994; Bryan *et al.*, 1995; Mazziotta *et al.*, 1995; Subsol *et al.*, 1996; Thompson *et al.*, 1997; Davatzikos, 1998; Resnick *et al.*, 2000; Rueckert *et al.*, 1999), using different spatial normalization methods. Methods for spatial normalization can be divided into volume-based, which try to

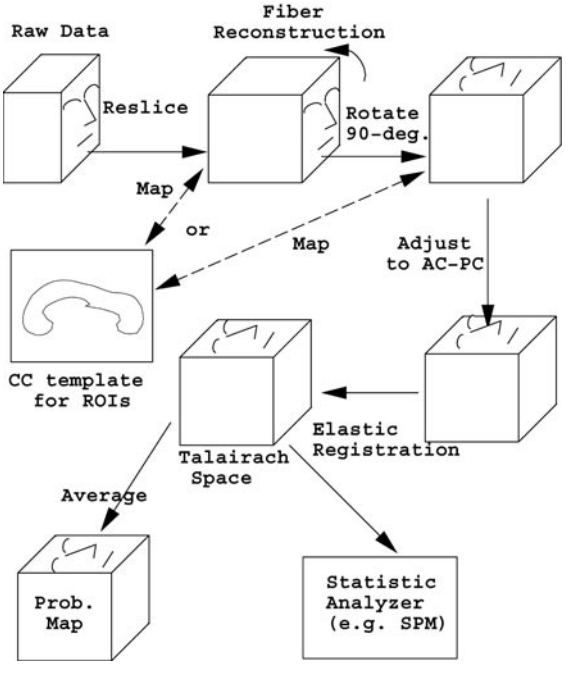

FIG. 2. Description of our framewrok for analyzing neural fiber distribution. The ROIs on the corpus callosum (CC) template are mapped to the midsagittal slice of each individual subject, either before or after rotation, depending on the user's selection.

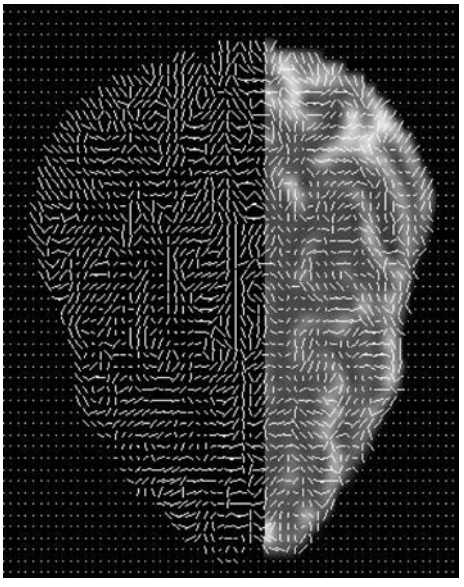

FIG. 3. A representative cross section of the DTI's primary eigenvector direction, half of which is overlaid on its corresponding intensity image.

match image intensities across subjects (Gee *et al.*, 1993; Collins *et al.*, 1994; Friston *et al.*, 1995a; Christensen *et al.*, 1996; Thirion, 1998; Freeborough and Fox, 1998; Rueckert *et al.*, 1999), and feature-based, which extract features such as structure boundaries, sulci, and gyri from MR images and subsequently determine 3D transformations that match these features (Davatzikos *et al.*, 1996; Thompson and Toga, 1996; Davatzikos, 1997a; Vaillant and Davatzikos, 1999; Ferrant *et al.*, 1999; Shen *et al.*, 2001). Combinations of the two approaches have also been described (Joshi *et al.*, 1995). More recent work on deformable matching applied on tensor fields of DT images can be found (Alexander *et al.*, 1999a,b, 2000, 2001; Alexander and Gee, 2000; Gee and Bajcsy, 1998). In this paper we use a high-dimensional elastic transformation, which is based in part on geometric features extracted from brain boundaries.

Generation and visualization of statistical fiber maps usually comprises three steps: first, fiber tracking based on the underlying tensor image; second, spatial normalization, which accounts for interindividual morphological variability and places tracked fibers into a stereotaxic space; and third, visualization of fiber bundles. We present each of these steps next. A schematic diagram is provided in Fig. 1.

It is important to note that if spatial normalization is capable of completely aligning white matter structures, then there is no residual variability. In practice, this is not the case, for two reasons. First, the spatial normalization method might not be able to completely remove interindividual variability, particularly in the cortex. Second, the white matter anatomy does not fully agree with the gray matter anatomy, particularly in variable cortical regions. Since we use SPGR images to obtain the spatial normalization transformation, we expect to have residual variability due to both of these factors. This poses a major challenge in precisely interpreting probabilistic maps. Our premise is that in the presence of disease, these maps are altered locally depending on the structures affected. Therefore, even though the probabilistic map reflects a composite of registration error and residual variability after alignment of gray matter structures, it can still help identify group differences corresponding to anatomical changes due to disease or normal development and aging.

METHODS

Figure 2 is a graphical description of our framework in practice, corresponding to the schematic diagram. Reslicing, rotation, and anterior commissure–posterior commissure (AC-PC) adjustment are some of the preprocessing steps before elastic registration, to increase image resolution and registration accuracy. Fiber reconstruction is performed on the double-sliced images. After all fibers of interest have been registered, they are ready to be analyzed by any available statistics tools, such as SPM. As an example, we create a probabilistic map of fiber distribution in the white matter passing through five ROIs. In the following subsections, key issues of this framework are to be addressed.

Processing DT Images

Diffusion tensor imaging measures microscopic diffusion along six independent directions and this results in a symmetric tensor **D** measured on each image voxel. Suppose that λ_1, λ_2, and λ_3 ($\lambda_1 \geq \lambda_2 \geq \lambda_3$) are the three eigenvalues of **D**. Then the *anisotropic factor* or *fractional anisotropy* FA is defined as (Poupon *et al.*, 1998)

$$\mathrm{FA} = \frac{3}{2} \times \left(\frac{\lambda_1}{\mathrm{trace}([D])} - \frac{1}{3}\right) \qquad (1)$$

or (Pierpaoli *et al.*, 1996)

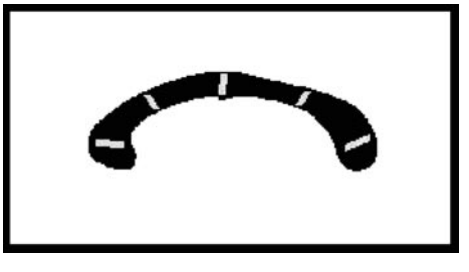

FIG. 4. A corpus callosum template and five ROIs selected to be far enough from each other so that corresponding fibers of single or multiple subjects can be visualized distinctly.

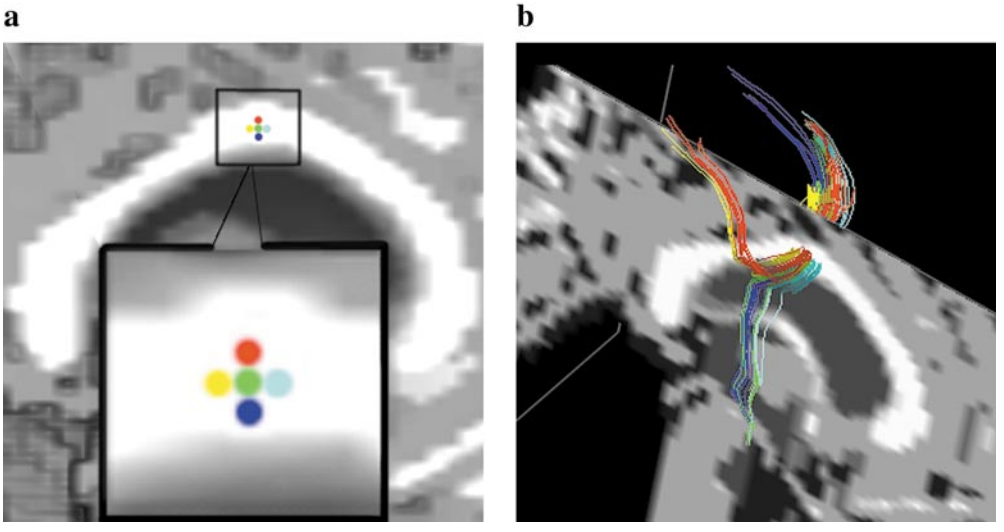

FIG. 5. Demonstration of tracking sensitivity to small error in placing the ROI. (a) Five neighboring voxels as small ROIs. (The actual size of the ROIs may be smaller than displayed.) (b) 3D view of five tracked fiber bundles passing through the five sample voxels.

$$FA = \sqrt{\frac{(\lambda_1 - \lambda_2)^2 + (\lambda_2 - \lambda_3)^2 + (\lambda_3 - \lambda_1)^2}{2 \times (\lambda_1^2 + \lambda_2^2 + \lambda_3^2)}}, \quad (2)$$

where a fully anisotropic tissue has a factor FA = 1.0 since trace[D] = λ_1, and an isotropic tissue has a factor FA = 0.0 since $\lambda_1 = \lambda_2 = \lambda_3$. The eigenvector $\mathbf{v_1}$ corresponding to λ_1 is the *primary direction* (PD). Figure 3 is a view of the primary direction of one brain slice projected to a 2D plane, in which part of the vector field is overlaid on its corresponding MR image.

Configuring Regions of Interest

Probabilistic maps are often shown as "fuzzy" images, the fuzziness of which reflects residual variability after some global registration that accounts for gross morphological differences (Evans *et al.*, 1993; Thompson *et al.*, 1997). An analogous way of generating probabilistic maps of fiber bundles is to account for overall shape variability via spatial normalization and record the residual variability of fiber bundles. However, the tremendous complexity of the white matter architecture would make this approach practically unusable if the atlas would be generated as a whole, because different fiber bundles of different individuals would appear highly mixed and overlapping in the stereotaxic space, which would result in most of the useful information being buried by the complexity.

The purpose of our work is to provide a tool that helps the study on a particular region or certain structures at a given region. In order to be able to visualize individual white matter pathways, and demonstrate the procedure of our framework, we choose to randomly define several ROIs simultaneously, which are well separated in each subject's volumetric image. We track only the fibers passing through those ROIs. As the tracked fibers form a fuzzy image reflecting interindividual variability in the stereotaxic space, they are well separated and therefore distinctly visualized.

Defining ROIs in each subject's images would in general be very laborious and subjective. Therefore, we have chosen a different approach. In particular, we defined five representative ROIs in the major callosal subdivisions of an atlas, and we transferred these ROIs to each subject's images via an elastic matching procedure, which adapted the shape of the atlas to the shape of each individual's corpus callosum. Fiber tracking was then initiated in those five ROIs in each subject. Figure 4 shows the five ROIs overlaid on the corpus callosum template. We defined the ROIs as strips orthogonal to the rostral–caudal axis of the callosum, since small errors in placing the ROI in the corpus callosum can lead to significantly deviating fibers. Figure 5 illustrates the sensitivity of fiber tracking to small error in placing ROIs. As shown in Fig. 5, left, we

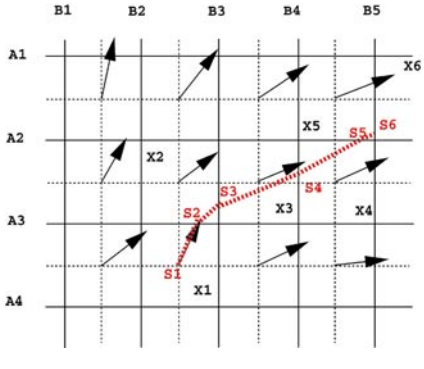

FIG. 6. Illustration of fiber tracking. Black arrows are the vector field and red dashed route is the tracked fiber tract.

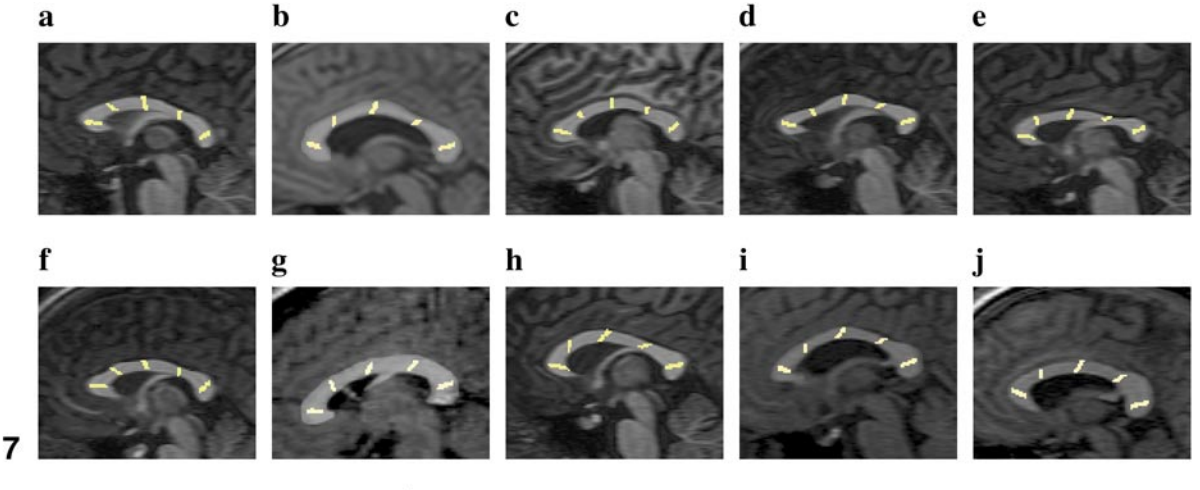

7

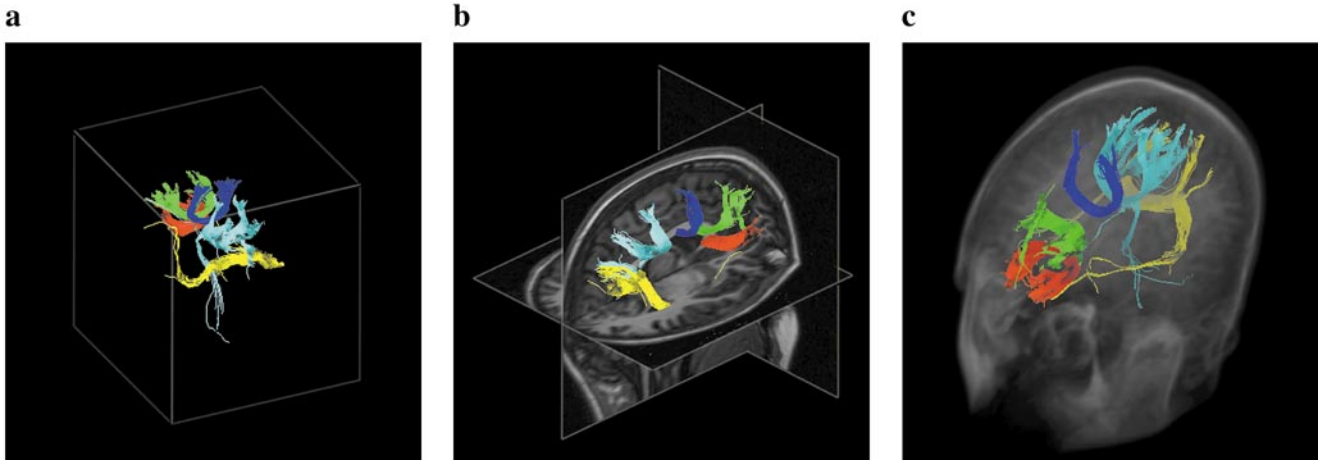

8

FIG. 7. The five regions of interest of Fig. 4 mapped to images of 10 subjects via elastic warping.
FIG. 8. One example of the fibers in original subject space: (a) the fibers alone, (b) the fibers incorporated into the subject's triplanar image display, and (c) the fibers embedded in the volume-rendered brain.

randomly selected five neighboring voxels that form a cross on the middle sagittal slice of corpus callosum and color coded them. Although the outer four voxels were just one voxel away from the center green voxel, the corresponding fibers differed from each other significantly: red and yellow followed dorsal directions while the other followed ventral directions. In order to mitigate this unwanted effect, we chose ROIs that are strips along the dorsal–ventral direction. By examining fibers passing through these well-separated dorsal–ventral strips, we can look at all callosal projections at a certain level in the rostral–caudal direction.

Fiber Extraction and Tracking

As described above, the primary direction, i.e., the direction of the principal eigenvector, of the diffusion tensor at each location tends to be along the direction of the fiber passing through that location. This is because water diffuses preferentially along the axis of the fiber. Fiber tracking is the process of following the flow field of these principal eigenvectors, thus generating trajectories of fiber bundles.

One could, in principle, start from a particular ROI and follow the direction of the principal eigenvector, thus following the corresponding fiber. However, at a branching point of the fiber, this algorithm would be forced to follow one or the other branch, depending on which branch has orientation that is most similar to the fiber orientation at the branching point. In order to avoid this unwanted situation, we have adopted a different procedure that is revised from Stieltjes *et al.* (2001). In particular, we initiate tracking of the principal eigenvectors from every single voxel in a subject's image. We then examine which of the reconstructed trajectories pass through the five callosal ROIs, and we retain all of them. For a branching fiber, this procedure reconstructs all branches of the fiber, one for each respective starting location.

Due to the error and noise in measurement, such as the partial-voxel effect, tracking is likely to deviate

from the true fiber track and orientation. To reduce this possibility, we track on a continuous coordinate system rather than a discrete voxel-based grid. Suppose a track lasts all the way until the current point; its connectivity at the next position is judged based on the occurrence of sudden transitions in the fiber orientation, quantified by R and C,

$$C = |\vec{\mu}_{\mathrm{L}} \cdot \vec{\mu}_{\mathrm{L}-1}|, \tag{3}$$

$$R = \sum_{i}^{s} \sum_{j}^{s} \mathrm{abs}(\vec{u}_i \cdot \vec{u}_j)/s(s-1), \tag{4}$$

$$\vec{u}_i = \mathrm{FA}_i \cdot \vec{\mu}_{\mathrm{L}}, \tag{5}$$

where vector $\vec{\mu}_{\mathrm{L}}$ is the unit vector at the current location, and $\vec{\mu}_{\mathrm{L}-1}$ is the unit vector at the voxel prior to the current on the tracked fiber; s is the number of the voxels referred in the neighborhood, $\vec{u}_k$ is a vector obtained by scaling a unit vector along the PD at the voxel by the local anisotropy FA value. R actually judges the local connectivity in a statistical sense, so that the tracking procedure is more robust in a noisy environment. C judges the transition smoothness; a lower threshold for C may result in high fiber curvature. Fiber tracking terminates whenever either the magnitude of anisotropy is too low or the direction of the vector field changes more than a prespecified threshold, i.e., either R or C is smaller than certain threshold values. In our experiment, we did not directly threshold the anisotropy FA value. We set $C >$ 0.7 (approximately 45°) to prevent fibers from sudden transition and used a value around 0.10 for R to keep tracking based on the connectivity of the neighborhood.[1]

The vector at each voxel represents the PD of a local tensor. Since we start tracking from anywhere in the volume, both positive and negative of this vector stand for a possible orientation. This causes a problem when it is necessary to interpolate at a nonmeasuring point, since tensor is measured only at the center of a voxel. To solve this problem, we perform the tracking based on voxels rather than on the measuring grids. In Fig. 6, the dashed lines describe the measuring grids, and the solid lines plot the voxels, which are the respective *influence territory* of each vector.

Let X_i denote a voxel, $\mathbf{v}_i$ the vector associated with X_i, and S_i a point position. If the tracking starts from the center of X_1, then the tracking algorithm can be described as follows:

Step 1 Initialize $i := 1$; mark the center of voxel X_1 as S_1.
Step 2 Take the positive direction of $\mathbf{v}_i$ at voxel X_i, as the current direction **d.**
Step 3 Starting from S_i, track along direction **d,** until the tract hits a boundary of this voxel X_i, at point S_{i+1}.
Step 4 If X_i is a voxel at the edge of the volume or either C or R is less than its threshold, stop; else, proceed to Step 5.
Step 5 Let $i := i + 1$: mark the voxel, at the other side of the boundary just hit, as X_i.
Step 6 If $\mathbf{v}_i$ at point S_i leads to inside of voxel X_i, **d** $:= \mathbf{v}_i$; else, **d** $:= -\mathbf{v}_i$.
Step 7 Goto Step 3.

This algorithm completes half of the tract tracking starting from point S_1. Taking the negative of $\mathbf{v}_1$ as initial direction **d** and repeating Step 3–Step 7 will reveal the other half of the same fiber tract.

In the example shown in Fig. 6, starting from point S_1, we can recover the fiber tract passing points $S_2, \ldots, S_6$ sequentially for the first half as shown by the red dashed line. Obviously, this algorithm allows several fibers to share one common voxel, and this is considered as fiber branches which meet the actual situation. To make this point more clear, it may be noticed that if we started the tracking from a point on the regions of interest, then there would be only one fiber connecting with this start point, while the reverse tracking would result in a bunch of fibers going through it, and this latter case reflects the reality. In Fig. 6, the black solid arrows represent the vector field.

Registration to the Atlas and Generation of the Probabilistic Fiber Map

Fibers tracked in each individual's images passing through ROIs, as described in the previous section, are spatially normalized into Talairach space, via an elastic image warping procedure (Davatzikos *et al.*, 1996; Davatzikos, 1997b), so that their variability can be visualized after the confounding effect of overall shape differences across individuals is factored out. We now summarize the steps involved in this procedure, referred to as STAR (spatial transformation algorithm for registration). STAR determines the elastic transformation that matches the outer (cortical) and inner (ventricular) boundaries of the brain parenchyma. The outer cortical boundary is reconstructed as a parameterized surface via a shrink-wrapping procedure (Davatzikos and Bryan, 1996), i.e., a procedure starting with an elastic surface that deforms into conformation with the shape of the individual brain. From the dif-

[1] Suppose FA > 0.5 stands for good directionality, and 45° for good smoothness, then an average of $0.5 \times 0.5 \times \cos(45°) \approx 0.177$ would be a good R threshold. Nevertheless, in our experiment we used $R =$ 0.10, which generated threadlike realistic fiber bundles, perhaps due to errors introduced during the multistep data preprocessing procedure.

ferential geometric characteristics of this surface, such as the principal curvatures, a map between the outer cortical surface of the subject and its counterpart in the Talairach atlas is determined, so that regions of similar geometric structure are mapped to each other (e.g., temporal lobes and occipital and frontal tips). A similar procedure matches the ventricular boundaries. Finally, the cortical and ventricular correspondences determined this way are used to drive a 3D elastic warping transformation, which tightly matches outer and inner parenchymal boundaries, while it propagates these boundary deformations internally by solving the elastic transformation equations.

This procedure is applied to the T_1-weighted, standard spoiled grass (SPGR) images. The resulting 3D warping field is then applied to the coregistered images of the fiber bundles, placing them into Talairach space.

After spatial normalization to the atlas space, a probabilistic map of each fiber is defined as the percentage of subjects having a particular fiber at a particular location in Talairach space.

TEN-SUBJECT PROBABILITY MAP OF CALLOSAL FIBER ROIs

In order to demonstrate the procedure of our framework for generating callosal fiber distribution maps, we collected SPGR images as well as DTI images from 10 young normal volunteers. The coregistered SPGR images were used as reference for deriving the warping transformations.[2]

All studies were performed using a 1.5-T Philips Gyroscan NT system. Diffusion-weighting imaging was accomplished using multislice segmented echo-planar imaging (EPI) with cardiac triggering (TR = 5 heart beats; TE = 92 ms) and navigator echo-phase correction (motion correction). A data matrix of 128 × 95 over a field of view of 230 × 173 mm was obtained acquiring 17 echoes per excitation. Slice thickness was 3 mm (52–60 slices) without gaps. From these consecutive multislice data, 3D volumes were reconstructed. Diffusion weighting was performed along six independent axes, using a b value of 600 s/mm^2 at the maximum gradient strength of 2.1 G/cm. A reference image with the least diffusion weighting was also recorded. The slices were acquired in an interleaved fashion and a single set of these seven measurements took 5–8 min. These measurements were repeated six times to increase the signal-to-noise ratio.

During the EPI-DTI acquisition, as a matter of fact, the anatomical distortion is one of the largest problems. The amount of the B_0 distortion heavily depends on the number of echoes acquired for each scan. For example, single-shot EPI acquires 64–128 echoes for each scan. While it is the fastest method, the amount of the distortion is also the largest. The distortion decreases dramatically as the number of echoes decreases. For example, two-shot EPI has half the length of the echo train (32–64). However, DTI studies based on the multishot EPI (non-single-shot) suffer from severe artifacts due to physiological motions (pulsation and respiration) and involuntary bulk motions. Because of this reason, the vast majority of DTI studies have been done using the single-shot EPI knowing the severe image distortion is a trade-off. Our laboratory has been working on the implementation of multishot EPI-based DTI techniques for the past several years. Our strategy is based on navigator-echo-based phase monitoring and phase correction. We also investigated the relationship between the image degradation and cardiac cycle to find the best cardiac triggering timing. Mori *et al.* (2000) and Stieltjes *et al.* (2001) are the published parts of our recent progress in this field. These technical developments allowed us to use four-shot EPI (17 echo acquisition/scan) and very well settled down the distortion correction issue.

Acquired data were processed on a SUN Enterprise computer. Images were first realigned using UCLA's AIR program (Woods *et al.*, 1998a,b), in order to remove any potential small bulk motions that occurred during the scans. Subsequently, all individual images were visually inspected to discard slices with motion artifacts. After the image quality check, the pixel intensities of the multiple diffusion-weighted images were fitted using multivariate linear least-square fitting to obtain the six elements of the symmetric diffusion tensor. The diffusion tensors at each voxel were diagonalized to obtain eigenvalues and eigenvectors.

The dimensions of the images were 256 × 256 × Z, and Z varied from 52 to 60 slices with nominally interpolated xy resolution of 0.9766 mm and Z resolution of 3.0 mm.

Five strips were defined as ROIs in the template, as shown in Fig. 4, and were subsequently transferred to each of the 10 subjects via elastic warping, as shown in Fig. 7. Fiber tracking was then initiated from each voxel of each subject's volumetric image. All fiber tracts that passed through any of these ROIs were maintained, which included all pertinent branches. And, all were reoriented parallel to the AC–PC line, prior to elastic warping to the atlas space. Figure 8 shows one example of the extracted fibers from 1 of the 10 subjects, in the subject's native space. Bundles of different ROIs are displayed in different colors. Figure 8a shows only the fibers, and the subject is viewed approximately from the rear of the left ear. Figure 8b shows the fiber tracts overlaid on a triplanar view of that subject's SPGR images. Figure 8c shows the same fibers overlaid on the volume-rendered SPGR image. Figure 8 also shows the sensitivity of callosal fiber

[2] Informed consent was obtained in accordance with guidelines specified by the local internal review board.

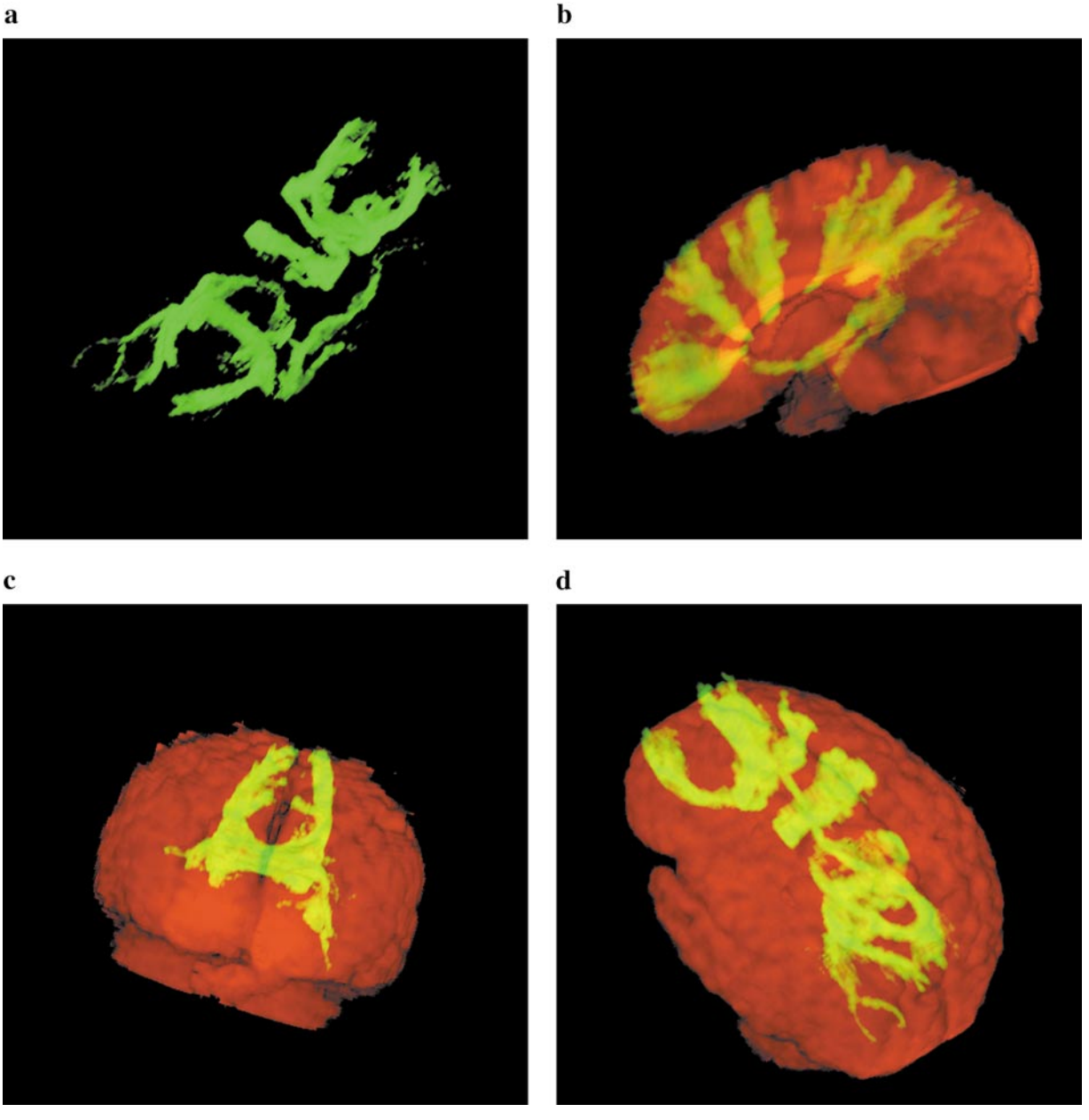

FIG. 9. Fiber bundles of subject (e) in Fig. 7 in atlas space. (a) Axial view of the warped fibers alone. (b) Sagittal view of the fibers embedded in an atlas brain. (c) Coronal view of the fibers embedded in the volume of an atlas brain. (d) Lateral view with atlas brain volume, viewed from rear upper left of the brain.

tracking with respect to the placement error of the ROI. A slight shift of the ROI along the dorsal–ventral direction can lead to different fibers. We chose ROIs that are in the form of dorsal–ventral strips, so as to include all fibers passing through a particular rostral–caudal position.

The fibers reconstructed from each subject's images were subsequently elastically warped to a digitized version of the Talairach atlas. The same transformations were used to warp the respective SPGR images of the same subject. The resulting spatially normalized fiber tract images, with values varying from 0.0 to 1.0 after trilinear interpolation, were averaged in a voxel-wise fashion to produce the probabilistic fiber map, whereas the spatially normalized SPGR images were averaged to produce the corresponding average brain, which was used as reference for the display of the fibers. Figure 9 displays the normalized fibers corresponding to the subject shown in Fig. 7e. The fibers are shown in Talairach space, after elastic warping. Figures 9b–9d show the same fiber bundles overlaid on the average brain. The sagittal view in Fig. 9b shows that

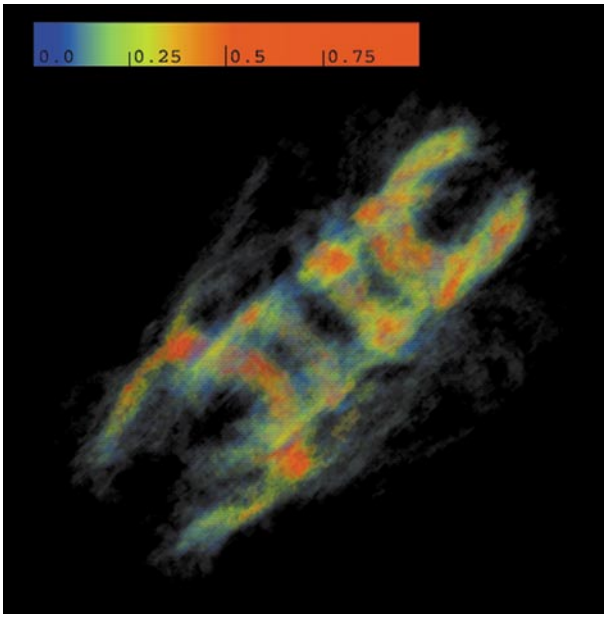

FIG. 10. Axial view of the color-coded probability map of 10 subjects (probability threshold at 0.1).

all five bundles of fibers pass through the five callosal ROIs.

Figure 10 shows the probability of the five fibers color-coded; for clarity, we present only the regions in which the probability of a fiber was higher than 0.1. After thresholding at 0.4, we see in Fig. 11a the main fiber stems of the five bundles. Figures 11b–11d show the 10-subject probabilistic fiber distribution viewed from orientations similar to those of the individual fibers in Fig. 9.

In order to assess the residual variability of gray matter morphology, which is a confounding factor in assessing true fiber variability, we formed the average T_1 image of the same subjects, by applying the spatial transformation of each subject to the respective T_1 image and averaging the resulting images. A triplanar section through the average T_1 volumetric image is shown in Fig. 12.

From Fig. 12 we see that the corpus callosum is relatively clear, implying a rather low residual variability, which is consistent with the tightness of the average fiber maps in the five callosal ROIs. More variable cortical structures, however, which appear fuzzy, are bound to cause a wider spread of fibers projecting on them. Ideally, these ROIs should be perfectly aligned, but because of the error during warping for registration, they deviate. In order to measure the registration accuracy in callosal region, we first warped the five ROIs on the corpus callosum template as displayed in Fig. 4 to the Talairach space brain. Then, following the route as described in Figs. 1 and 2 that generated the warped fibers of the 10 individuals, we obtained another set of five ROIs, which were also defined in the Talairach space. A perfect registration would match these two sets of five ROIs. However, by measuring the sample coincidence of the five ROIs point-wise, a demonstration of the ROI registration accuracy is shown in Fig. 13, in which A–E give the deviations along *xyz* at the five sampling locations, and F is the average deviation of all samples in the five ROIs. The resolution of the subjects is 0.9766 $\times$ 0.9766 $\times$ 3.0 mm, but we measure the registration error in Talairach space, the resolution of which is 0.87 $\times$ 0.87 $\times$ 2.0 mm. We can see that the largest variation is at B(x) $\approx$2.01 voxels $\approx$1.75 mm, B(y) $\approx$4.27 voxels $\approx$3.71 mm, and E(z) $\approx$2.46 voxels $\approx$4.92 mm. Since the dimension is 256 $\times$ 256 $\times$ 57 voxels, the maximal deviations in *xyz* are about 0.8, 1.7, and 4.3%, and the average deviations (F) in the three directions are about 1.30, 2.56, and 3.55 mm, which is 0.6, 1.1, and 3.1%. The z axis here is actually along the corpus callosum's dorsal–ventral direction, bearing relatively larger registration error. This observation supports our selection of ROIs to be strips along the dorsal–ventral direction. A more detailed analysis of registration error for STAR can be found in Davatzikos (1997a), which showed that the average cortical registration error was 3.4 mm (standard deviation 2.1 mm and maximum 10.4 mm) and the average subcortical registration error was 2.5 mm (standard deviation 1.6 mm and maximum 8.5 mm).

DISCUSSION

We have presented a practical framework for constructing probabilistic maps of the spatial distribution of white matter tracts, using diffusion tensor imaging coupled with high-dimensional spatial normalization methods. We have applied this procedure to images from 10 healthy young volunteers and reconstructed maps of the distribution of callosal fibers. In addition, the normalized subjects and generated probability maps from this framework are ready for further analysis by any other available tools such as SPM.

These experiments demonstrated on a group of 10 healthy normal subjects that DTI, in conjunction with fiber tracking algorithms, can produce reproducible across-subject reconstructions of fiber pathways. These reconstructions have previously been shown to be in qualitative agreement with neuroanatomical knowledge of interhemispheric projections (Stieltjes *et al.*, 2001; Mori *et al.*, 2000; Xue *et al.*, 1999a,b). Our experiments also showed that statistical averaging across subjects can smooth out individual variance and also potential errors that might be caused by the fiber reconstruction algorithms. A comparison of Fig. 9 with Figs. 10 and 11, particularly at the optic radiations level, shows this fact. Importantly, regions which might display high error levels, perhaps due to high level of noise of the underlying vector field, or due to

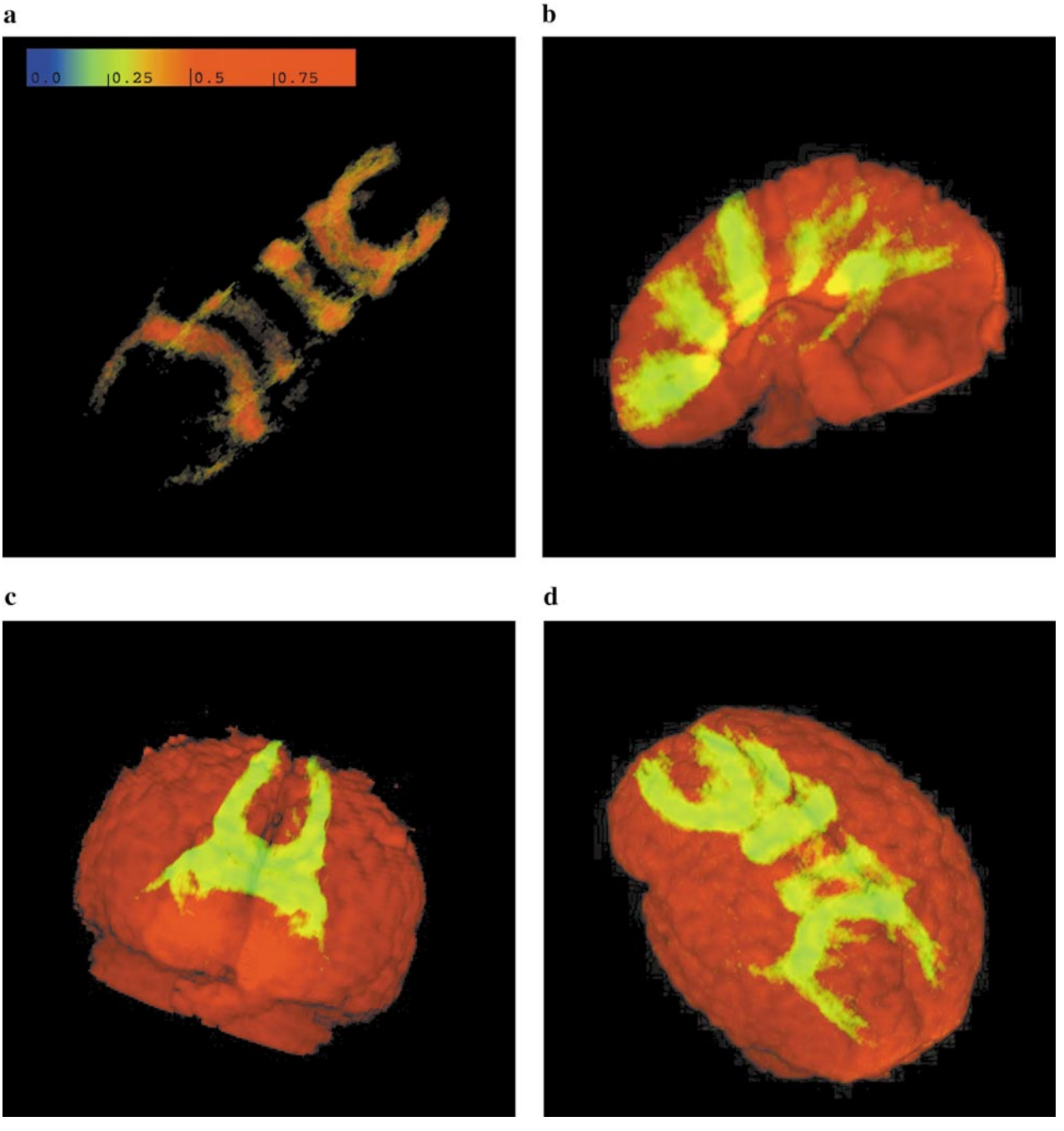

FIG. 11. Probability map of 10 subjects (displayed in the average SPGR brain space, thresholded at 0.4). (a) Axial view. (b) Sagittal view. (c) Coronal view. (d) Lateral view.

anatomical complexity and a mixture of different fibers that results in unreliable fiber tracking, could potentially be determined by the analysis of normative data such as the ones generated in this work, thereby guiding the interpretation of fibers extracted from individual subjects.

A confounding factor in population analysis of fiber pathways is the residual variability of gross morphology after spatial normalization. This confounding effect is particularly prominent around variable cortical folds. More accurate deformable registration methods (Shen and Davatzikos, 2002; Tao *et al.*, 2001; Davatzikos *et al.*, 2001) will ultimately reduce this confounding effect. As displayed in Fig. 12 by the representative slices of the average SPGR image, and by comparing the registration error statistics in callosal, cortical, and subcortical areas, our experiments showed that registration errors are constantly smaller in the corpus

callosum, where the ROIs for fiber tracking initialization were placed. An extensive quantitative assessment of these errors, and therefore of residual morphological variability, must be undertaken in the future. We qualitatively assessed this error by forming images of the average gross morphology, after spatial normalization of the respective T_1 images. The fuzziness of these images reflects residual variability of cortical and subcortical structures. These images can be used in conjunction with the probabilistic fiber maps for better interpretation of individual variability of callosal projections.

Our results showed that these new techniques are promising to help elucidate brain connectivity via *in vivo* magnetic resonance imaging and should be able to assist in understanding how brain connections change with development, aging, and disease. These results are part of an ongoing study to establish normative data for fiber pathways. Population differences can then be quantified by statistically comparing the respective probabilistic maps. For example, techniques analogous to statistical parametric mapping (Friston *et al.*, 1995b) can be applied on spatially normalized fiber maps, in order to identify regions in which brain connectivity is affected by disease. Similarly, probabilistic maps of the underlying vector fields can be analyzed, thus eliminating potential errors of the fiber reconstruction step. Work toward these directions is under way in our laboratory.

Currently, it takes about 40 min to warp one image of the size mentioned under Ten-Subject Probability Map. We are also working to shorten this computational expense by parallelizing the algorithm.

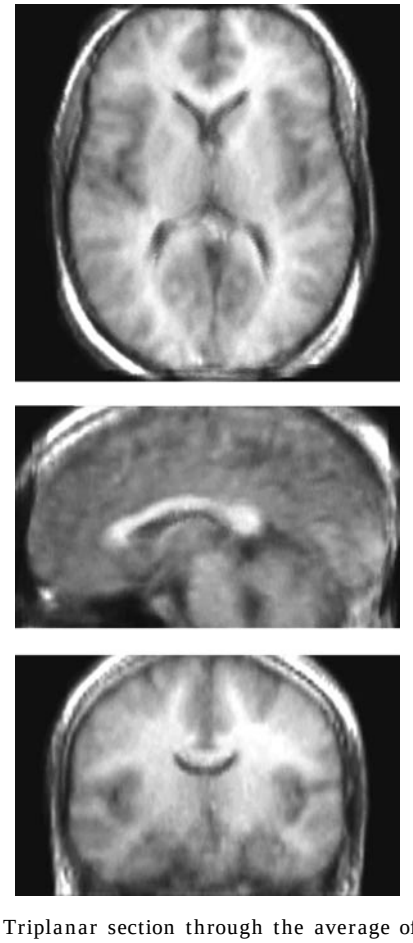

FIG. 12. Triplanar section through the average of 10 spatially normalized T_1 images, reflecting residual variability of gray matter structures.

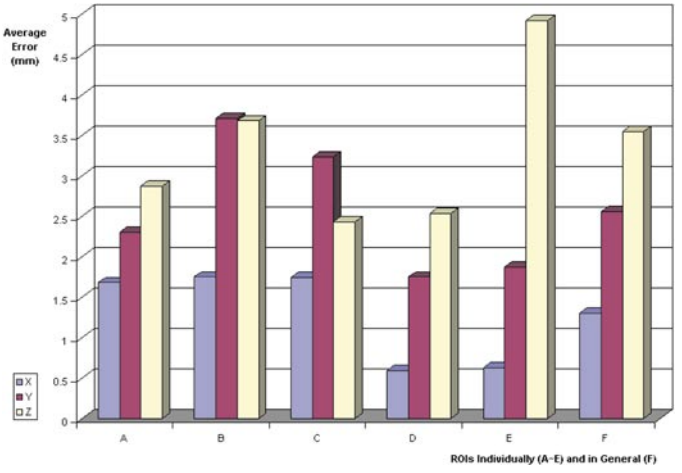

FIG. 13. Average error distribution of our registration method. Sagittal view is on *zy* plane, and coronal view is on *zx* plane. A–E are the errors on five ROIs, and F is the error in general on these five ROIs.

ACKNOWLEDGMENTS

The authors thank Dr. Henli Li for his help. This work was supported in part by NIH Grant ROI AG14971-04 and by NIH/NCRR Center Grant P41 RR15241.

REFERENCES

Alexander, D. C., and Gee, J. C. 2000. Elastic matching of diffusion tensor images. *Comput. Vision Image Understand.* **7:** 233–255.

Alexander, D. C., Gee, J. C., and Bajcsy, R. 1999a. Transformations of and similarity measures for diffusion tensor MRI's. In *Proc. Int. Workshop Biomedical Image Registration* (F. Pernus, S. Kovacic, H. S. Stiehl, and M. Viergever, (Eds.), pp. 127–136.

Alexander, D. C., Gee, J. C., and Bajcsy, R. K. 1999b. Strategies for data reorientation during nonrigid warps of diffusion tensor images. In *Proc. MICCAI'99,* pp. 463–472.

Alexander, D. C., Pierpaoli, C., Basser, P. J., and Gee, J. C. 2000. Techniques for spatial normalization of diffusion tensor images. In *Proc. SPIE Medical Imaging* (K. M. Hanson, Ed.), pp. 470–481.

Alexander, D. C., Pierpaoli, C., Basser, P. J., and Gee, J. C. 2001. Spatial transformations of diffusion tensor magnetic resonance images. *IEEE Trans. Med. Imaging* **20:** 1131–1139.

Basser, P. J., Pajevic, S., *et al.* 2000. In vivo fiber tracktography using DT-MRI data. *Magn. Res. Med.* **44:** 625–632.

Bates, E., and Elman, J. L. 1993. Connectionism and the study of change. In *Brain Development and Cognition: A Reader* (M. H. Johnson, Ed.), pp. 623–642. Blackwell, Oxford.

Baumgardner, T. L., Singer, H. S., Denckla, M. D., Rubin, B. S., Abrams, B. A., Colli, M. J., and Reiss, A. L. 1996. Corpus callosum morphology in children with Tourette syndrome and attention deficit hyperactivity disorder. *Neurology* **47:** 477–482.

Beaton, A. A. 1997. The relation of planum temporal asymmetry and morphology of the corpus callosum to handedness, gender and dyslexia: A review of the evidence. *Brain Lang.* **60:** 255–322.

Bishop, K. M., and Wahsten, D. 1997. Sex differences in the human corpus callosum: Myth or reality? *Neurosci. Biobehav. Rev.* **21:** 581–601.

Bookstein, F. L. 1996. Biometrics, biomathematics, and the morphometric synthesis. *Bull. Math. Biol.* **58:** 313–365.

Bryan, R. N., Davatzikos, C., Vaillant, M., Prince, J. L., Letovsky, S. Raghavan, R., Nowinski, W., Salamon, G., Murayama, N., Levrier, O., and Zilbovicius, M. 1995. Creation of population-based anatomic atlases with a brain image database. In *First Int. Conf. on Functional Brain Mapping,* p. 72. [Abstract]

Christensen, G. E., Rabbitt, R. D., and Miller, M. I. 1996. Deformable templates using large deformation kinematics. *IEEE Trans. Image Process.* **5**(10): 1435–1447.

Clarke, S., Kraftsik abd Van der Loos, H. R., and Innocenti, G. M. 1989. Forms and measures of adult and developing human corpus callosum. *J. Neuropathol. Exp. Neurol.* **280:** 213–230.

Collins, D. L., Neelin, P., Peters, T. M., and Evans, A. C. 1994. Automatic 3D intersubject registration of MR volumetric data in standardized Talairach space. *J. Comput. Assisted Tomogr.* **18:** 192–205.

Conturo, T. E., Lori, N. F., Cull, T. S., *et al.* 1999. Tracking neuronal fiber pathways in the living human brain. *Proc. Natl. Acad. Sci. USA* **96:** 10422–10427.

Davatzikos, C. 1997a. Spatial transformation and registration of brain images using elastically deformable models. *Comp. Vision Image Understand.* **66:** 207–222.

Davatzikos, C. 1997b. Spatial transformation and registration of brain images using elastically deformable models. *Comput. Vision Image Understand.* **66:** 207–222.

Davatzikos, C. 1998. Mapping of image data to stereotaxic spaces: Applications to brain mapping. *Hum. Brain Mapping* **6:** 334–338.

Davatzikos, C., and Bryan, R. N. 1996. Using a deformable surface model to obtain a shape representation of the cortex. *IEEE Trans. Med. Imaging* **15:** 785–795.

Davatzikos, C., Genc, A., Xu, D., and Resnick, S. M. 2001. Voxel-based morphometry using the RAVENS maps: Methods and validation using simulated longitudinal atrophy. *NeuroImage* **14:** 1361–1369.

Davatzikos, C., Vaillant, M., Resnick, S. M., Prince, J. L., Letovsky, S., and Bryan, R. N. 1996. A computerized method for morphological analysis of the corpus callosum. *J. Comput. Assisted Tomogr.* **20:** 88–97.

DeLacoste-Utamsing, M. C., and Holloway, R. L. 1982. Sexual dimorphism in the human corpus callosum. *Science* **216:** 1431–1432.

Evans, A. C., Collins, D. L., Mills, S. R., Brown, E. D., Kelly, R. L., and Peters, T. M. 1993. 3D statistical neuroanatomical models from 305 MRI volumes. In *Proc. IEEE Nuclear Science Symposium and Medical Imaging Conf.* **3:** 1813–1817.

Ferrant, M., Warfield, S. K., Guttmann, C. R. G., Mulkern, R. V., Jolesz, F. A., and Kikinis, R. 1999. 3D image matching using a finite element based elastic deformation model. In *Proc. MICCAI'98,* pp. 202–209.

Freeborough, P. A., and Fox, N. C. 1998. Modeling brain deformations in Alzheimer's disease by fluid registration of serial MR images. *J. Comput. Assisted Tomogr.* **22:** 838–843.

Friston, K. J., Ashburner, J., Frith, C. D., Poline, J. B., Heather, J. D., and Frackowiak, R. S. J. 1995a. Spatial registration and normalization of images. *Hum. Brain Mapping* **2:** 165–189.

Friston, K. J., Holmes, A. P., Worsley, K. J., Poline, J. P., Frith, C. D., and Frackowiak, R. S. J. 1995b. Statistical parametric maps in functional imaging: A general linear approach. *Hum. Brain Mapping* **2:** 189–210.

Gee, J. C., Reivich, M., and Bajcsy, R. 1993. Elastically deforming 3D atlas to match anatomical brain images. *J. Comput. Assisted Tomogr.* **17:** 225–236.

Gee, J. C., and Bajcsy, R. K. 1998. Elastic matching: Continuum mechnical and probabilistic analysis. In *Brain Warping* (A. W. Toga, Ed.). Academic Press, New York.

Giedd, J. N., Castellanos, F. X., *et al.* 1994. Quantitative morphology of the corpus callosum in attention deficit hyperactivity disorder. *Am. J. Psychiatry* **151:** 665–669.

Greitz, T., Bohm, C., and Eriksson, L. 1991. A computerized brain atlas: Construction, anatomical content, and some applications. *J. Comput. Assisted Tomogr.* **15:** 26–38.

Huppi, P. S. 2001. MR imaging and spectroscopy of brain development. *Magn. Reson. Imaging Clin. North Am.* **9:** 1–17.

Janowsky, J. S., Kaye, J. A., and Carper, R. A. 1996. Atrophy of the corpus callosum in Alzhemier's disease versus healthy aging. *Am. Geriatr. Soc.* **44:** 798–803.

Joshi, S. C., Miller, M. I., Christensen, G. E., Banerjee, A., Coogan, T., and Grenander, U. 1995. Hierarchical brain mapping via a generalized Dirichlet solution for mapping brain manifolds. In *Proc. SPIE Conf. on Geometric Methods in Applied Imaging* **2573:** 278–289.

Mazziotta, J. C., Toga, A. W., Evans, A., Fox, P., and Lancaster, J. 1995. A probabilistic atlas of the human brain: Theory and rationale for its development. *NeuroImage* **2:** 89–101.

Miller, M. I., Christensen, G. E., Amit, Y., and Grenander, U. 1993. Mathematical textbook of deformable neuroanatomies. *Proc. Natl. Acad. Sci. USA* **90:** 11944–11948.

Mori, S., Crain, B. J., Chacko, V. P., and van Zijl, P. C. M. 1999. Three-dimensional tracking of axonal projections in the brain by magnetic resonance imaging. *Ann. Neurol.* **45:** 265–269.

Mori, S., Itoh, R., Zhang, J., Kaufmann, W. E., van Zijl, P. C. M., Solaiyappan, M., and Yarowsky, P. 2001a. Diffusion tensor imaging of the developing mouse brain. *Magn. Reson. Med.* **46:** 183–188.

Mori, S., Kaufmann, W. E., Davatzikos, C., Stieltjes, B., Amodei, L., Fredericksen, K., Pearlson, G. D., Melhem, E. R., Solaiyappan, M., Raymond, G. V., Moser, H. W., and van Zijl, P. C. M. 2001b. Imaging cortical association tracts in the human brain using diffusion-tensor-based axonal tracking. *Magn. Reson. Med.* **47**(2): 215–223.

Mori, S., Kaufmann, W. E., Pearlson, G. D., Crain, B. J., Stieltjes, B., Solaiyappan, M., and van Zijl, P. C. M. 2000. In vivo visualization of human neural pathways by magnetic resonance imaging. *Ann. Neurol.* **47:** 412–414.

Neil, J. J., Shiran, S. I., McKinstry, R. C., Schefft, G. L., Snyder, A. Z., Almli, C. R., Akbudak, E., Aronovitz, J. A., Miller, J. P., Lee, B. C., and Conturo, T. E. 1998. Normal brain in human newborns: Apparent diffusion coefficient and diffusion anisotropy measured by using diffusion tensor mr imaging. *Radiology* **209:** 57–66.

O'Sullivan, M., Jones, D. K., Summers, P. E., Morris, R. G., Williams, S. C. R., and Markus, A. S. 2001. Evidence for cortical disconnection as a mechanism of age-related cognitive decline. *Neurology* **57:** 632–638.

Pfefferbaum, A., Sullivan, E. V., Hedehus, M., Lim, K. O., Adalsteinsson, E., and Moseley, M. 2000. Age-related decline in brain white matter anisotropy measured with spatially corrected echo-planar diffusion tensor imaging. *Magn. Reson. Med.* **44:** 259–268.

Pierpaoli, C., Jezzard, P., Basser, P. J., Barnett, A., and Di Chiro, G. 1996. Diffusion tensor MR imaging of human brain. *Radiology* **201:** 637–648.

Poupon, C., *et al.* 1998. Regularization of MR diffusion tensor maps for tracking brain white matter bundles. In *MICCAI'98,* pp. 489–498.

Poupon, C., Clark, C. A., Froulin, V., *et al.* 2000. Regularization of diffusion-based direction maps for the tracking of brain white matter fascicles. *NeuroImage* **12:** 184–195.

Resnick, S. M., Goldszal, A., Davatzikos, C., Golski, S., Kraut, M. A., Metter, E. J., Bryan, R. N., and Zonderman, A. B. 2000. One-year age changes in MRI brain volumes in older adults. *Cereb. Cortex* **10:** 464–472.

Roland, P. E., Graufelds, C. J., Wahlin, J., *et al.* 1994. Human brain atlas: For high-resolution functional and anatomical mapping. *Hum. Brain Mapping* **1:** 173–184.

Rueckert, D., Sonoda, L. I., Hayes, C., Hill, D. L. G., Leach, M. O., and Hawkes, D. J. 1999. Non-rigid registration using free-form deformations: Application to breast MR images. *IEEE Trans. Med. Imaging* **18:** 712–721.

Shen, D., Herskovits, E., and Davatzikos, C. 2001. An adaptive-focus statistical shape model for segmentation and shape modeling of 3D brain structures. *IEEE Trans. Med. Imaging* **20**(4): 257–270.

Shen, D., and Davatzikos, C. 2001. HAMMER: Hierarchical attribute matching mechanism for elastic registration. In *Proc. Intl. Workshop on Mathematical Methods in Medical Imaging* (L. Staib, Ed.), Kauai, HI, USA, December, pp. 29–36.

Stieltjes, B., Kaufmann, W. E., van Zijl, P. C. M., Pearlson, G. D., and Mori, S. 2001. Diffusion tensor imaging and axonal tracking in the human brainstem. *NeuroImage* **14:** 723–735.

Subsol, G., Thirion, J. Ph., and Ayache, N. 1996. Application of an automatically built 3D morphometric brain atlas: Study of cerebral ventricle shape. In *VBC '96, Lecture Notes in Computer Science* (K. H. Hohne, Ed.), September, pp. 373–382. Springer-Verlag, Hamburg.

Tao, Xiaodong, Han, Xiao, Rettmann, M. E., Prince, J. L., and Davatzikos C. 2001. Statistical study on cortical sulci of human brains. In *17th Int. Conf. on Information Processing in Medical Imaging* (R. M. Leahy and M. F. Insana, Eds.), pp. 475–487. Springer-Verlag, Berlin.

Thirion, J. P. 1998. Image matching as a diffusion process: An analogy with Maxwell's daemons. *Med. Image Anal.* **2:** 243–260.

Thompson, P. M., Giedd, J. N., Woods, R. P., MacDonald, D., Evans, A. C., and Toga, A. W. 1999. Dynamic growth and pruning patterns in the developing human brain identified using continuum-mechanical tensor mapping. In *5th Int. Conf. on Functional Mapping of the Human Brain,* Dusseldorf, Germany.

Thompson, P. M., MacDonald, D., Mega, M. S., Holmes, C. J., Evans, A. C., and Toga, A. W. 1997. Detection and mapping of abnormal brain structure with a probabilistic atlas of cortical surfaces. *J. Comput. Assisted Tomogr.* **21:** 567–581.

Thompson, P., and Toga, A. W. 1996. A surface-based technique for warping three-dimensional images of the brain. *IEEE Trans. Med. Imaging* **15:** 402–417.

Vaillant, M., and Davatzikos, C. 1999. Hierarchical matching of cortical features for deformable brain image registration. *Lect. Notes Comput. Sci. Inf. Process. Med. Imaging* **1613:** 182–195.

Vermersch, P., Roche, J., Hamon, M., Daems-Monpeurt, C., Pruvo, J. P., Dewailly, P., and Petit, H. 1996. White matter magnetic resonance imaging hyperintensity in Alzheimer's disease: Correlations with corpus callosum atrophy. *Neurology* **243:** 231–234.

Woods, R. P., Grafton, S. T., Holmes, C. J., Cherry, S. R., and Mazziotta, J. C. 1998a. Automated image registration. I. General methods and intrasubject, intramodality validation. *J. Comput. Assisted Tomogr.* **22:** 141–154.

Woods, R. P., Grafton, S. T., Watson, J. D. G., Sicotte, N. L., and Mazziotta, J. C. 1998b. Automated image registration. II. Intersubject validation of linear and nonlinear models. *J. Comput. Assisted Tomogr.* **22:** 155–165.

Woodruff, P. W. R., Pearlson, G. D., Geer, M. J., Barta, P. E., and Chilcoat, H. D. 1993. A computerized magnetic resonance imaging study of corpus callosum morphology in schizophrenia. *Psychol. Med.* **23:** 45–56.

Xue, R., van Zijl, P. C. M., Crain, B. J., Solaiyappan, M., and Mori, S. 1999a. In vivo three-dimensional reconstruction of rat brain axonal projections by diffusion tensor imaging. *Magn. Reson. Med.* **42:** 1123–1127.

Xue, R., van Zijl, P. C. M., and Mori, S. 1999b. Brain axonal projection reconstruction by rapid 3D diffusion MRI. In *Exerpta Medica Intern. Congress Series* (S. Naruse and H. Watari, Eds.), pp. 199–200.